The Institute of Space and Astronautical Science
Report No. 663, March 1996

Symmetric Baroclinic Instability of Modified Hadley-Cell Models

By
Ho Sang KWAK and Kunio KUWAHARA
(February 16, 1996)

ABSTRACT : A numerical investigation is made of symmetric instability of baroclinic flows in a finite domain of horizontal fluid layer. A modified rotating Hadley-cell flow configuration is designed to achieve $Ri \leq O(1)$ by constructing two models, i.e., in Model I, $\Delta T_v = 0$; and in Model II, the free-slip and thermally-insulated upper boundary is adopted. A finite-volume numerical procedure is utilized to integrate the fully-nonlinear time-dependent Navier-Stokes equations over broad parameter ranges, i.e., the thermal Rossby number $1.0 \leq Ro \leq 40.0$, and the Richardson number $0.2 \leq Ri \leq 2.0$. The *Ro-Ri* diagram illustrates three flow regimes: (1) the stable flow regime with respect to the symmetric baroclinic instability, (2) the steady symmetric baroclinic wave regime, and (3) the vacillating symmetric baroclinic wave regime. The critical Richardson number for stability is determined and overall energetics of finite amplitude symmetric baroclinic waves are illustrated. The large-time behavior of wave generation is examined, and a plausible physical interpretation is offered. Both the time-dependent characteristics and the energetics of the vacillating symmetric baroclinic waves are scrutinized. Discussions are given on the impact of the nonlinear effects of symmetric baroclinic waves on the basic-state flow field.

1. INTRODUCTION

Instabilities of a geostrophically-balanced baroclinic zonal (azimuthal) flow have been a classical topic [*1*]. The accumulated knowledge clearly suggests that a stably stratified baroclinic flow may be destabilized by several different mechanisms. The most widely studied type of instability has been the (conventional) geostrophic baroclinic instability, which is known to take place at large Richardson numbers. For this instability, the fastest growing perturbation has a dominant zonal structure; this feature has been demonstrated in the laboratory, and a substantial body of information has been compiled. It is now recognized that the wavy cyclone and anticyclone pair in the mid-latitude atmosphere is caused by this type of instability.

Another type of instability, termed symmetric baroclinic instability (hereafter referred to as SBI), has been thought to occur for small Richardson number $Ri \leq O(1)$ [*2,3*]. For this, the fastest-growing disturbances have a primarily meridional structure, with no or only weak zonal structure. SBI is understood to be triggered by a combined action of buoyancy and inertial restoring forces [*1*]. For a simple inviscid zonal flow which contains a constant horizontal density gradient, this basic flow is stable for $0 < Ri < 1$, but it can be unstable if the inertial and convective influences act together. If viscosity and thermal diffusion are added, the above two effects are damped; the relative damping of these two effects depends on the Prandtl number [*4,5*]. The role of SBI has been discussed in a number of different geophysical contexts: the banded structure of Jupiter's atmosphere [*6*], and the organized meso-scale convective rolls in Earth's atmosphere [*7,8*], to name a few. The existence of SBI has been conjectured for some time, however, conclusive physical evidence of SBI has been elusive both in natural observations and in laboratory experiments. This inconclusiveness of the subject has perhaps revived interest in SBI in recent years [*9,10*].

Because of the difficulty involved in experimental realizations, modern research of SBI has been

directed to analytical/numerical approaches using simple baroclinic flow models. A benchmark configuration was an infinite confined horizontal fluid layer subjected to a constant horizontal temperature gradient. Stone [*11,12*] considered a three-dimensional stability problem of the Eady model. In this configuration, the upper and lower horizontal boundaries move with the local zonal velocities so that a uniform vertical velocity shear is sustained by the thermal wind relation. Admittedly, the problem formulation appears to be somewhat artificially contrived; however, owing to this simplification, no boundary layers exist in the basic state. Furthermore, even in the perturbation analyses, viscous and thermal diffusion effects were neglected.

Efforts to introduce viscous and thermal diffusion effects in the Eady model were made [*8,13*]. A more realistic basic-state flow was proposed by Antar & Fowlis [*14*], which was termed the rotating Hadley cell. In this model, a fluid layer confined between two horizontal plates of infinite extent is considered. These two horizontal plates are co-rotating, and a constant temperature gradient is imposed on the two horizontal boundaries. It was shown that, if the velocity and temperature gradients are independent of y (the south-north direction), an exact closed-form solution to the Navier-Stokes equations is available. It is notable that this basic state contains both the Ekman and thermal boundary layers. Antar & Fowlis [*3*] calculated the linear growth rate of three-dimensional perturbations of the Hadley cell in some ranges of the characteristic parameters, i.e., the Prandtl number Pr, the thermal Rossby number Ro, the Ekman number E and the vertical temperature difference ΔT_v. It was found that for the cases $Pr \neq 1$, SBI dominated for $Ri < 0.675$, but SBI was not detected even for a lower range $0.3 < Ri < 0.8$ for the case of $Pr = 1$. Furthermore, it was pointed out that the symmetric modes with maximum growth rate were not strictly symmetric; rather, they had weak zonal structures. However, the preceding analytical approaches did not deal with the nonlinear (or finite-amplitude) effects; also, no analysis was given of the energetics of the flow.

Serious attempts to acquire numerical solutions to the full Navier-Stokes equations were made by several authors. In particular, Miller [*4*] obtained finite-difference numerical solutions for fully-nonlinear symmetric waves for the Eady and Hadley cell models for $Ri \sim O(1)$. Miller elaborated that the primary energy source for SBI is : (1) the conversion from the potential energy via vertical motions and temperature correlation if $Pr > 1$, (2) from the mean kinetic energy by virtue of an induced meridional flow if $Pr < 1$, and (3) from both of the above two if $Pr = 1$. The main thrust of the work of Miller was placed on revealing the qualitative character of symmetric baroclinic waves; therefore, no detailed parameter studies were given. The parameter space that was covered in the above investigations was not broad enough to assess the full impact of finite-amplitude effects.

Parallel endeavors have been made on the experimental front. The vertically-mounted cylindrical annulus with differential sidewall heating was extensively studied [*15*]. However, the Richardson number was not an externally-specifiable parameter in this experimental apparatus. Typically, the resulting Ri was large so that SBI was suppressed. Stone et al. [*16*] and Hadlock et al. [*17*] designed a new annulus such that horizontal temperature gradients were applied on the conducting upper and lower endwalls. Furthermore, for this annulus, the vertical temperature difference ΔT_v between the two horizontal plates was externally controllable. The advantage of this apparatus is that the Richardson number can be made to be small. This experimental setup can be described to be a realistic realization of the above-stated rotating Hadley cell model. It was asserted that SBI was detected in this configuration; however, the validity of this assertion was subsequently questioned because of the lack of detailed and definitive measurements. An improved version of this type of apparatus was used later by Miller & Fowlis [*18*] and Hathaway & Fowlis [*19*]. The results of these more recent experiments identified characteristic flow regimes in the parameter space of the thermal Rossby number and the Taylor number for several values of ΔT_v. However, no elucidating evidence of SBI was found. These experiments observed a Benard-like instability even in the range of small Ri. It is important to recall that, for the Hadley-cell model, the Richardson

number can be expressed as $Ri \cong Pr + 4\Delta T_v/Ro$ when $E<<1$. The working fluid in these experiments was water with $Pr\sim7$. Consequently, in order to accomplish the condition $Ri \leq O(1)$, a large negative value of ΔT_v was needed. This implies that the system was strongly heated at the bottom so that a Benard-type instability was activated in the horizontal boundary layers. Accordingly, SBI was suppressed. This phenomenon was addressed by Quon [*20*] in his numerical simulations of the flow in an annulus apparatus of this type. Miller [*4*] also monitored unsteady vacillating flows in the rotating Hadley cell due to this type of instability. In summary, no convincing evidence to ascertain the existence of SBI has appeared in the literature. Difficulties are enormous in achieving the condition $Ri \leq O(1)$, without having to cause associated disturbances, in the experimental and/or numerical problem formulation.

The above background review suggests that a key element of laboratory research for SBI lies in the design of a flow configuration which would accomplish the condition $Ri \leq O(1)$ with minimum possibilities of exciting other instabilities. The objective of the present study is to devise simple baroclinic flow models to satisfy this requirement. Two models are being considered. The first one, referred to as Model I, represents a specific case of the rotating Hadley cell model, with the imposed vertical temperature difference $\Delta T_v = 0$. It can be shown that, for this case, the approximate Richardson number in the interior becomes a function of the Prandtl number only, under the assumption $E<<1$. The other one, termed Model II, is essentially a modified Hadley cell model in that the no-slip and thermally-conducting conditions at the upper horizontal plate are replaced by the free-slip and thermally-insulating upper surface conditions. As in the case of the original Hadley cell model, Model II permits an exact closed-form solution to the Navier-Stokes equations for the basic state. In the basic state of Model II, the profiles of temperature and of zonal velocity are similar; also, the Richardson number can be expressed in the same functional form as for Model I. It is worth mentioning that the boundary conditions similar to those of Model II were considered by prior investigators [*8,10*]. It may be argued that the free-slip boundary condition, although not easily realizable in the laboratory, might be a better depiction of the real atmosphere since the artificially-placed solid wall has now been eliminated.

As stressed, a major impetus of the present models is that the approximate Ri is a function of Pr only. This implies that, by selecting an appropriate working fluid (thus, the Prandtl number), the Richardson number can be controlled by external means. This advantage may be appreciated by noting that, if a working fluid of $Pr \leq O(1)$ is chosen, the condition $Ri \leq O(1)$ may be readily achieved without having to introduce a negative vertical temperature difference ($\Delta T_v < 0$). This provides an ideal environment to capture SBI.

In the present paper, numerical experiments are conducted by employing a finite-volume method to integrate the fully-nonlinear Navier-Stokes equations. The mission is to simulate finite-amplitude symmetric baroclinic flows in a finite domain of horizontal fluid layer by imposing periodicity at the vertical boundaries. Calculations were performed in the parameter space of the thermal Rossby number $1 \leq Ro \leq 40$, while the Richardson number encompasses a range, $0.2 \leq Ri \leq 2.0$. Emphasis will be placed on searching for SBI by revealing the qualitative essentials of the characteristic flow regimes. By post-processing the numerical data, the flow structures and energetics of symmetric baroclinic waves will be scrutinized. Concern will be directed to analyzing the impact of the wave formation on the basic flow field, as they are interlinked by finite-amplitude nonlinear effects.

2. THE MODEL

Consider a Boussinesq fluid, which is confined between two horizontal plates, separated by h. The entire system rotates steadily about the vertical central axis z, which is antiparallel to gravity g, with a constant angular frequency Ω. It is assumed that the fluid layer is infinite in the horizontal

extent, and the domain of interest is far from the rotation axis. Based on these considerations, it is convenient to use rectangular Cartesian coordinates (x,y,z), which respectively point in the eastward, northward, and vertical directions. On the lower horizontal boundary surface, a constant temperature gradient in the y-direction, γ, is imposed. A schematic diagram of the configuration, together with the descriptions of Models I and II, is given in Fig. 1.

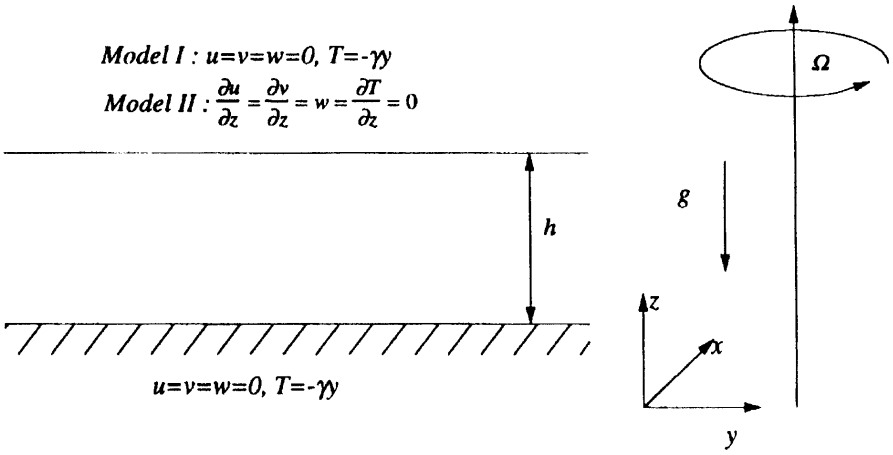

Fig. 1 Schematic diagram of Models I and II.

The governing Navier-Stokes equations, under the symmetric assumption $\partial/\partial x = 0$, may be written, in non-dimensional form and viewed in a rotating reference frame, as

$$\frac{\partial u}{\partial t}+Ro\left[\frac{\partial}{\partial y}(uv)+\frac{\partial}{\partial z}(uw)\right]-2v=E\nabla^2 u, \tag{1}$$

$$\frac{\partial v}{\partial t}+Ro\left[\frac{\partial}{\partial y}(v^2)+\frac{\partial}{\partial z}(vw)\right]+2u=-\frac{\partial p}{\partial y}+z+E\nabla^2 v, \tag{2}$$

$$\frac{\partial w}{\partial t}+Ro\left[\frac{\partial}{\partial y}(vw)+\frac{\partial}{\partial z}(w^2)\right]=-\frac{\partial p}{\partial z}+\theta+E\nabla^2 w, \tag{3}$$

$$\frac{\partial \theta}{\partial t}+Ro\left[\frac{\partial}{\partial y}(v\theta)+\frac{\partial}{\partial z}(w\theta)-v\right]=\frac{E}{Pr}\nabla^2\theta, \tag{4}$$

$$\frac{\partial v}{\partial y}+\frac{\partial w}{\partial z}=0, \tag{5}$$

where ∇^2 denotes the two-dimensional Laplacian operator. In the above, standard notation is employed, i.e., p is the pressure, T the temperature, t the time, and (u,v,w) the velocity components corresponding respectively to the (x,y,z) directions (note, in the above equations, θ indicates the periodic component of temperature, i.e., $T = \theta - y$). Nondimensionalization was effectuated by using h, U_0, $1/\Omega$, and γh as reference scales for length, velocity, time and temperature, respectively. Here, U_0 is the thermal wind velocity, i.e., $U_0 = \alpha g \gamma h/\Omega$, where α denotes the coefficient of thermometric expansion of the fluid. The relevant dimensionless parameters are the thermal Rossby number, $Ro=\alpha g\gamma/\Omega^2$; the Ekman number, $E=\nu/\Omega h^2$; the Pranftl number, $Pr=\nu/\kappa$.

In line with the model descriptions, the boundary conditions are stated :

for Model I, $u=v=w=\theta=0$ at $z=\pm 1/2$, (6)

for Model II, $u=v=w=\theta=0$ at $z=-1$, (7a)

$$\frac{\partial u}{\partial z}=\frac{\partial v}{\partial z}=w=\frac{\partial \theta}{\partial z}=0 \quad \text{at } z=0. \tag{7b}$$

It is important to point out that the basic state of the above two models admit closed-form analytical solutions under the assumptions that (1) the vertical gradients of both velocity and temperature are much larger than the horizontal ones, and (2) the vertical velocity component is negligibly small in comparison to the horizontal velocity components. These assumptions are justified on the grounds that the overall height of the fluid layer is much smaller than the horizontal length scale, and that the region of present interest lies far away from the rotation axis. Upon invoking the assumptions, (1)-(4) may be approximated as

$$-2v=E\frac{d^2u}{dz^2}, \tag{8}$$

$$2u=E\frac{d^2u}{dz^2}+z, \tag{9}$$

$$-v=\frac{E}{PrRo}\frac{d^2\theta}{dz^2}, \tag{10}$$

$$\theta=\frac{dp}{dz} \tag{11}$$

The stationary basic-state of Model II can be acquired as the analytical solutions to equations (8)-(11), with the boundary conditions of (7). These are

$$u(z)=\frac{1}{2}z+\frac{1}{2}g_1(z)-\frac{1}{4}g_2(z), \tag{12}$$

$$v(z)=-\frac{1}{2}f_1(z)+\frac{1}{4}f_2(z), \tag{13}$$

$$\theta(z)=\frac{PrRo}{2}\left\{\frac{1}{2}z+\frac{1}{2}g_1(z)-\frac{1}{4}g_2(z)\right\}, \tag{14}$$

where

$$\begin{aligned}
f_1(z) &= \{\sin R\,(1+z)\sinh R(1-z)+\sin R(1-z)\sinh R(z+1)\}/H(R),\\
g_1(z) &= \{\cos R\,(1+z)\cosh R(1-z)+\cos R(1-z)\cosh R(z+1)\}/H(R),\\
f_2(z) &= \{\cos R\,(2+z)\sinh Rz-\sin R(2+z)\cosh Rz\\
&\quad +\cos Rz\sinh R(2+z)-\sin Rz\cosh R(2+z)\}/RH(R),\\
g_2(z) &= \{\cos R\,(2+z)\sinh Rz+\sin R(2+z)\cosh Rz\\
&\quad +\cos Rz\sinh R(2+z)+\sin Rz\cosh R(2+z)\}/RH(R),
\end{aligned}$$

in which

$$H(R)=\cosh 2R+\cos 2R, \quad R\equiv E^{-1/2}.$$

It is evident in equations (12)-(14) that the velocities of the basic state are dependent on the Ekman number only. Exemplary velocity profiles are plotted in Fig. 2 over a wide range of E. Clearly, the flow field can be divided into two regions, i.e., the boundary layers and the interior region. In the interior, the zonal velocity increases almost linearly with height, and this trend becomes more conspicuous as E decreases. Obviously, this nearly-constant vertical velocity shear is sustained to balance the imposed constant horizontal temperature gradient, which points to the thermal-wind relation. The magnitude of the meridional velocity is nearly zero in much of the

interior. In the vicinity of the lower solid wall, an Ekman layer of thickness $O(E^{1/2})$ exists to match the no-slip condition. Near the upper free-surface, a weak boundary layer is seen, which adjusts the velocity components to the free-slip condition at the upper boundary.

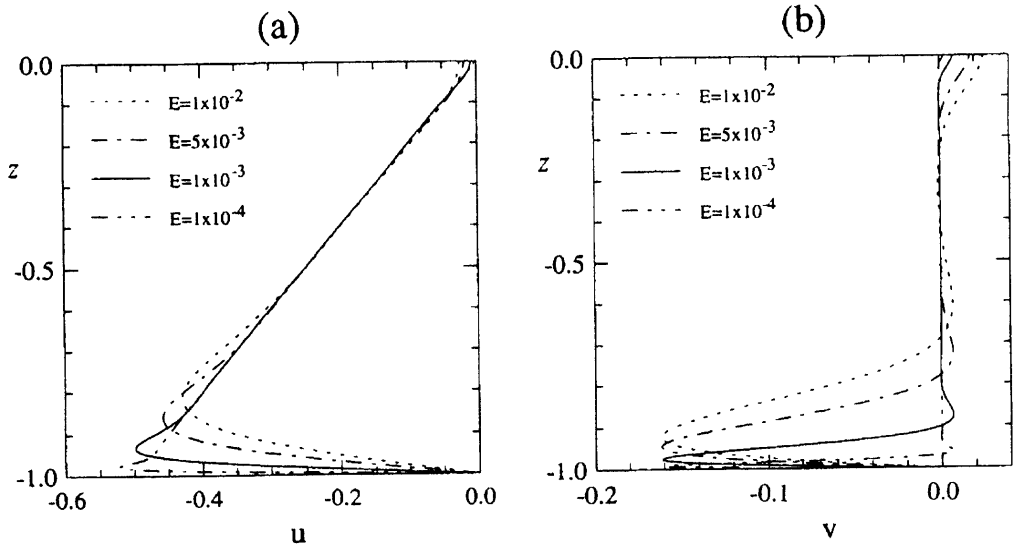

Fig. 2 The analytic basic state of Model II. Vertical profiles of (a) zonal velocity u, and (b) meridional velocity v

Inspection of (8) and (10) discloses that the profile of the basic-state temperature has the same functional form as that of u; the u-profile is identical to the θ-profile scaled by $PrRo/2$. Once the basic-state temperature profile is determined, the principal nondimensional parameter in the discussion of baroclinic instability, i.e., the Richardson number, Ri, can now be deduced as

$$Ri=\alpha g\left(\frac{\partial T^*}{\partial z^*}\right)\Big/\left(\frac{\partial u^*}{\partial z^*}\right)^2 \tag{15}$$

in which asterisk indicates dimensional quantities. Equation (15) clearly shows that Ri is, in general, a function of z.

In the original Hadley-cell model [*14*], in the interior region, the vertical gradients of the basic-state u and T are almost constant when E is very small. It then follows that, at mid-depths of the fluid layer, Ri can be approximated as

$$Ri\cong Pr+\frac{4\Delta T_v}{Ro}+O(E^{1/2}) \tag{16}$$

where ΔT_v denotes the vertical temperature difference between the two horizontal plates. For model I, $\Delta T_v=0$, thus, $Ri\cong Pr+O(E^{1/2})$.

Similar arguments prevail for Model II. Since the vertical temperature gradient and vertical shear of u are of the same shape and almost constant for small E, Ri in the interior becomes nearly independent of z. Consequently, in a similar manner to Antar & Fowlis [*14*], Ri for Model II can be deduced approximately :

$$Ri\cong Pr+O(E^{1/2}). \tag{17}$$

Notice that the approximate expression for Ri, as stated in (17) is identical for both Models I and II.

The main idea is the fact that Ri becomes a function of Pr only, when E is sufficiently small.

A finite-volume numerical procedure, based on the SIMPLER algorithm [*21*], was adopted to simulate the fully nonlinear symmetric baroclinic waves of Model I and II. Time-marching solutions were acquired by numerically integrating the unsteady equations (1)-(5). The second-order differencing methods were employed to gain high accuracy. For the first- and second-derivatives of the linear terms, the standard central differencing scheme was used. A QUICK scheme suggested by Hayase et al. [*22*], was selected for the nonlinear advection terms. This is known to reduce the artificial diffusivity which is associated with the standard first-order upwind scheme.

As stated earlier, in order to conduct numerical calculations in a finite horizontal domain, the assumption is that the solution is horizontally-periodic with the horizontal wavelength L. Accordingly, the periodic boundary conditions for u, v, w, p, and θ are imposed on the vertical walls which are L apart:

$$f(0, z, t) = f(L, z, t), \tag{18}$$

where f stands for a pertinent variable. Care was exercised in choosing the adequate size of L. Here, L should be large enough to accommodate the most-favored wavelengths for a given parameter set. At the same time, however, L should not be too large so that important short wavelengths are not inadequately resolved. In the present simulations, a rough size of L was initially selected by referring to the previous results of the original Hadley cell model [2,4,5]. Fine-tuning was conducted to narrow down the value of L on a trial and error basis to capture dominant wavy characteristics.

A staggered grid system was introduced. In particular, to resolve the thin horizontal boundary layers near the plates, at least five grid points were placed in the Ekman layer. The grid spacing was uniform in the horizontal direction. For most of the runs in the paper, (62x42) grid points in the (y,z) plane were used.

It is advantageous to introduce the equations governing the global transfer between the kinetic and potential energies, which may be derived as [23]:

$$\frac{\partial}{\partial t}\langle KE\rangle = \langle w'\theta'\rangle + \langle \bar{v}z\rangle + E\langle \mathrm{v}\cdot\nabla^2\mathrm{v}\rangle = \langle E_1\rangle + \langle E_2\rangle + \langle F\rangle, \tag{19}$$

$$\frac{\partial}{\partial t}\langle KE'\rangle = \langle w'\theta'\rangle - Ro\langle u'w'\frac{\partial \bar{u}}{\partial z}\rangle - Ro\langle v'w'\frac{\partial \bar{v}}{\partial z}\rangle + E\langle \mathrm{v}'\cdot\nabla^2\mathrm{v}'\rangle = \langle E_1\rangle + \langle E_3\rangle + \langle E_4\rangle + \langle F\rangle, \tag{20}$$

$$\frac{\partial}{\partial t}\langle \overline{KE}\rangle = \langle E_2\rangle - \langle E_3\rangle - \langle E_4\rangle + \langle \bar{F}\rangle, \tag{21}$$

$$\frac{\partial}{\partial t}\langle PE\rangle = -\langle w'\theta'\rangle - \langle \bar{v}z\rangle - \frac{E}{PrRo}\langle z\nabla^2\theta\rangle = \langle E_1\rangle - \langle E_2\rangle - \langle D\rangle. \tag{22}$$

In the above, $\bar{f}$ and $\langle f\rangle$ are defined to denote the horizontal and volume averages of a quantity f and f' is the deviation from the horizontal average, i.e., $f' = f - \bar{f}$. The total kinetic energy is KE [$\equiv(u^2+v^2+w^2)/2$], and the potential energy PE[$\equiv -zT/Ro$]. The terms $\langle E_1\rangle$ and $\langle E_2\rangle$ represent convective conversions between the wave kinetic energy and the potential energy, and between the horizontally-averaged kinetic energy and the potential energy, respectively. The nonlinear conversions, $\langle E_3\rangle$ and $\langle E_4\rangle$, are between the wave kinetic energy and the horizontally-averaged

kinetic energy. Note that, in the present convention, a positive sign of these terms implies that the energy conversion is from the latter to the former. Viscous and thermal dissipations are shown by $\langle F \rangle$ and $\langle D \rangle$, respectively.

3. RESULTS AND DISCUSSION

Numerical runs were made with a fixed value of $E=10^{-3}$ and for varying Ro and Pr. The stated goal was to simulate SBI, and, therefore, a range of small Pr, i.e., $0.2 \leq Pr \leq 2.0$, was encompassed. It is recalled that, in the present Models I and II, $Ri \approx Pr$ for $E \ll 1$, which implies that the condition $Ri \sim O(1)$ is fulfilled. The range of Ro was wide, i.e., $1.0 \leq Ro \leq 40.0$.

Time-marching integration was carried out to near-steady state conditions by using the aforementioned analytical basic-state as the initial conditions. In the course of integration, no artificial disturbances were added to the basic state. The computer round-off error was able to trigger the growth of waves by disturbing the basic state. If no growing modes of the perturbations are detected until the diffusion time scale $O(E^{-1})$, the system was judged to be stable. For these cases, the large-time behavior of the solution, such as the global energetics and the flow structures, remained virtually unchanged with time. These tasks were accomplished by continuously monitoring the temporal variations of the individual terms of equations (19)-(22). For some cases, an apparent steady state was not achieved; rather, quasi-steady temporarily-vacillating waves were observed. For these cases, computation was continued until the first dominant mode of wave evolution was fully damped out.

The computed cases are marked in the Ro-Ri diagram, as shown in Fig. 3. The essential qualitative character of flow can be classified into three major categories: (1) the regime in which the flow is stable to SBI, (2) the steady finite-amplitude symmetric baroclinic wave regime, and (3) the vacillating symmetric baroclinic wave regime. Here, regime (2) indicates a situation in which infinitesimal perturbations grow to develop steady symmetric baroclinic waves of finite amplitude.

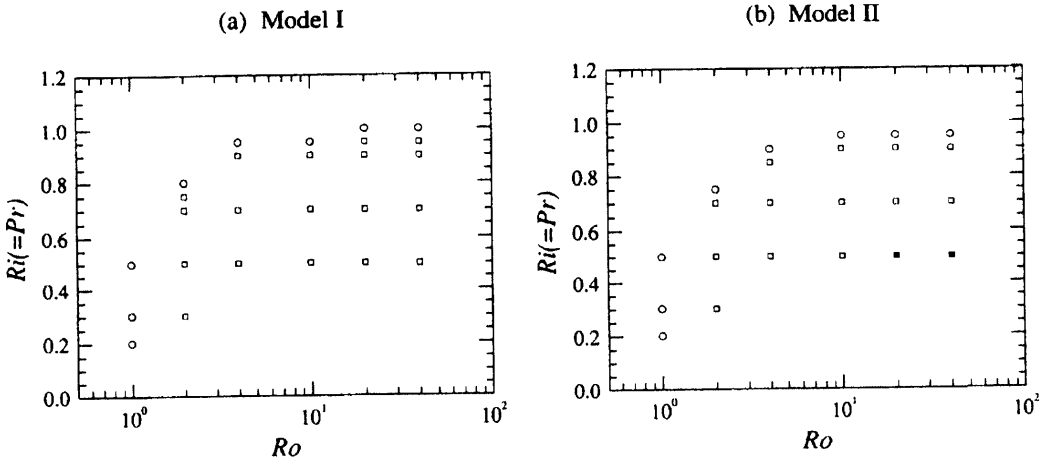

Fig. 3 Computed points in the Ro-Ri diagram for (a) Model I, and (b) Model II. In the figures, O represents the stable flow regime with respect to SBI;□, the steady symmetric baroclinic wave regime; ■, the vacillating symmetric baroclinic wave regime.

In the first, the question of the critical Richardson number Ri_C is raised. For a fixed value of Ro, when Ri exceeds Ri_C, the basic state is thought to be stable to symmetric perturbations. In the present numerical runs, the regime stable to SBI was determined by noting that the growth of two-dimensional disturbances was not detected even after the diffusive time scale. However, it should be stressed that this regime is stable to only SBI, and the conventional baroclinic instability can

occur in this parameter range [*3*]. In the present simulations, only discrete points in the parameter space were covered, which posed difficulties in evaluating the exact values of Ri_C. However, inspection of Fig. 3 leads to an approximate value of Ri_C for each run as well as to the associated global trends. In Fig. 3(a) for Model I, it is evident that, for $Ro \gg 1$, Ri_C is nearly independent of Ro, taking a value between 0.95 and 1.0. For small Ro, as Ro decreases (which implies an increasing rotation effect), Ri_C decreases. This observation is consistent with the assertion of Stone [*12*] that SBI is suppressed by non-hydrostatic influences.

The general shapes of the stability curves for Models I and II are in line with the results for the Eady model [*5,12*]. For small Ro, a quantitative difference in Ri_C is seen between the two models (see the values of Ri_C for Ro=2.0 and Ro=4.0). This is attributable to the difference in the upper boundary conditions. The ultimate source of energy of symmetric baroclinic waves is the potential energy [*4*]. As symmetric baroclinic waves are formed, the potential energy is reduced. This results in enhanced heat transfers from the horizontal boundaries, which, in turn, provide kinetic energy of the symmetric baroclinic waves. Model II has an insulated upper wall. This implies that the available heat transfer for Model II tends to be less than that of Model I in which both the upper and lower boundary walls are conducting. Based on this argument, Model II is seen to be more stable to SBI than Model I.

A set of representative plots showing the time evolution of the overall energetic properties of steady symmetric baroclinic waves is illustrated in Fig. 4 for Ro=2.0, Pr=0.5. As is evident in the plots, in the initial phase of wave generation, all of the averaged energetic properties exhibit an overshoot (energy barrier) before reaching an approximate equilibrium. Immediately after this overshoot, residual oscillations are seen; however, these oscillations are damped out after only a few cycles.

The large-time behavior of Fig. 4 indicates that the wave generation is intimately associated with the augmented heat transfer to the fluid, as previously asserted. The net heat transfer at the two horizontal boundaries for Model I is substantially enhanced by the presence of the waves. For Model II, heat transfer is augmented at the lower boundary. Because of this increased heat transfer, the potential energy of the horizontally-averaged state is lowered. Put it alternatively, both the horizontally-averaged and wave kinetic energies grow at the expense of potential energy. Further inspection of Fig. 4 is supportive of these arguments. In Fig. 4(d), $\langle E_2 \rangle$ and $\langle E_3 \rangle$ are dominant and they are comparable in magnitude; $\langle E_1 \rangle$ is relatively small and $\langle E_4 \rangle$ is negligible. A plausible physical explanation can be offered. The horizontally-averaged field gains its kinetic energy from the potential energy by inertial interactions denoted by $\langle E_2 \rangle$, and this, in turn, supplies the wave kinetic energy by way of the nonlinear interaction $\langle E_3 \rangle$. These interactions based on the energetics are consistent with the condition $Pr<1$ to capture symmetric baroclinic waves. In this situation, the buoyancy-restoring effect is damped more easily than the inertial effect. Thus, the buoyancy-induced conversion from the potential energy to the wave kinetic energy, represented by $\langle E_2 \rangle$, is less vigorous; on the contrary, the inertial effects, shown up in $\langle E_2 \rangle$ and $\langle E_3 \rangle$, are dominant [*4*]. These physical descriptions are applicable to the characteristics of symmetric baroclinic wave regime for both Models I and II.

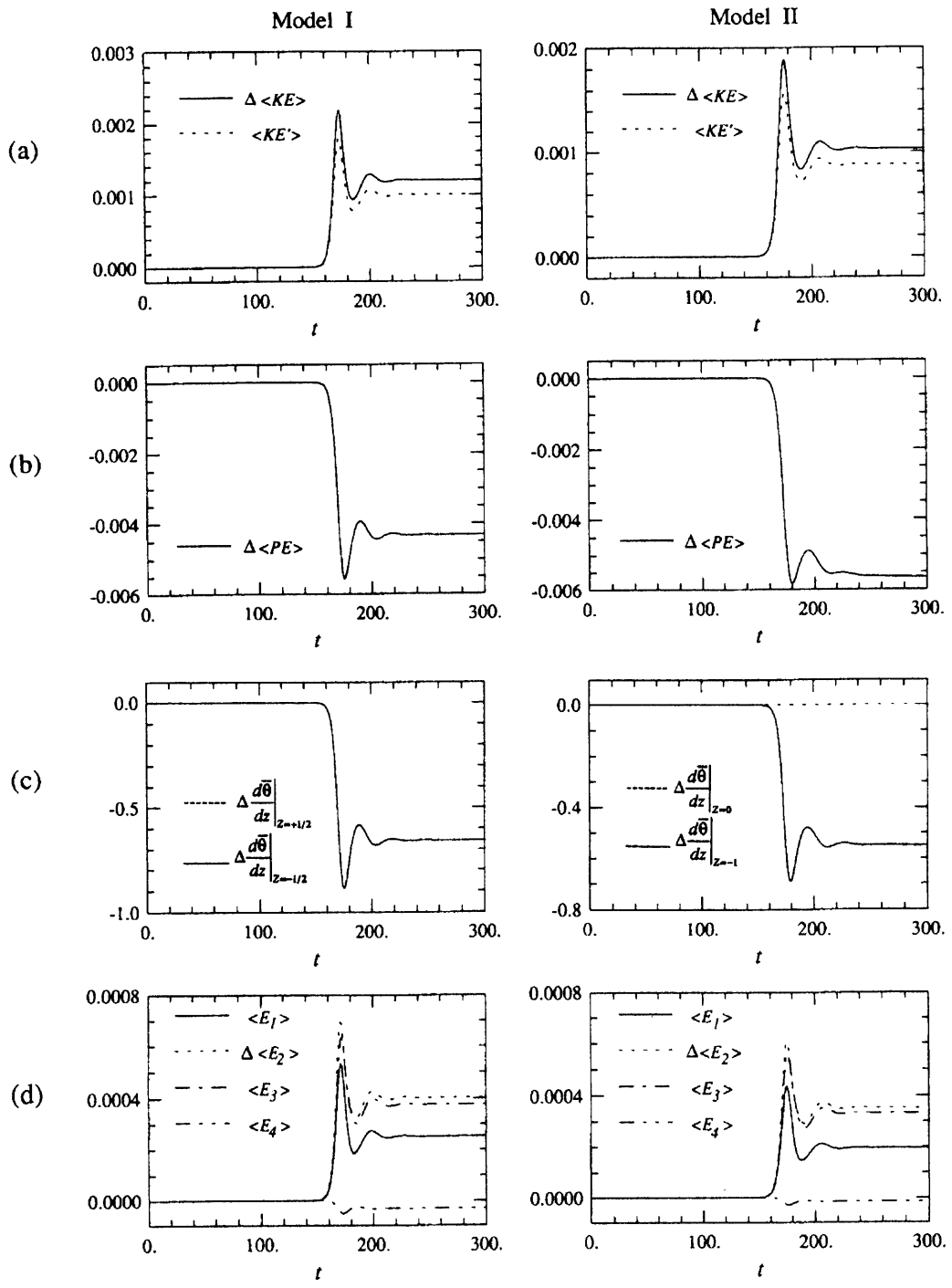

Fig. 4 Evolutions of the steady symmetric baroclinic wave energetics of Model I (left column) and of Model II (right column) for Ro =2.0 and Pr =0.5: (a) kinetic energies, $<KE>$ and $<KE'>$; (b) potential energy $<PE>$; (c) horizontally-averaged vertical temperature gradients at the upper and lower boundaries, $d\bar{\theta}/dz|_T$ and $d\bar{\theta}/dz|_B$; (d) equation terms in (19)-(22). Note that Δ denotes the deviation from the basic-state solution.

Temporal behavior of the local flow properties in the interior region is exemplified in Fig. 5. As is conspicuous in Fig. 5 (right column), the local properties of Model II, after reaching a quasi-equilibrium, display oscillatory patterns. When Ri is slightly less than Ri_C, this oscillatory pattern

closely resembles a sinusoidal form; however, as Ri falls further below Ri_C, distorted oscillatory patterns emerge. This temporal oscillatory behavior of the local properties may be interpreted to be a reflection of the fact that finite-amplitude symmetric baroclinic waves move in the horizontal direction with a nearly-constant speed. Here, it is emphasized that the flow is classified into the steady symmetric wave regime based on the invariance of the global characteristics, although the local properties are oscillatory.

In contrast to the case of Model II, the oscillatory tendency of the local variables for Model I at large times is hardly noticeable, as is evident in Fig. 5 (left column). Cross-comparisons of the results of the two cases underscore the importance of the upper boundary condition in inhibiting the occurrence of oscillation.

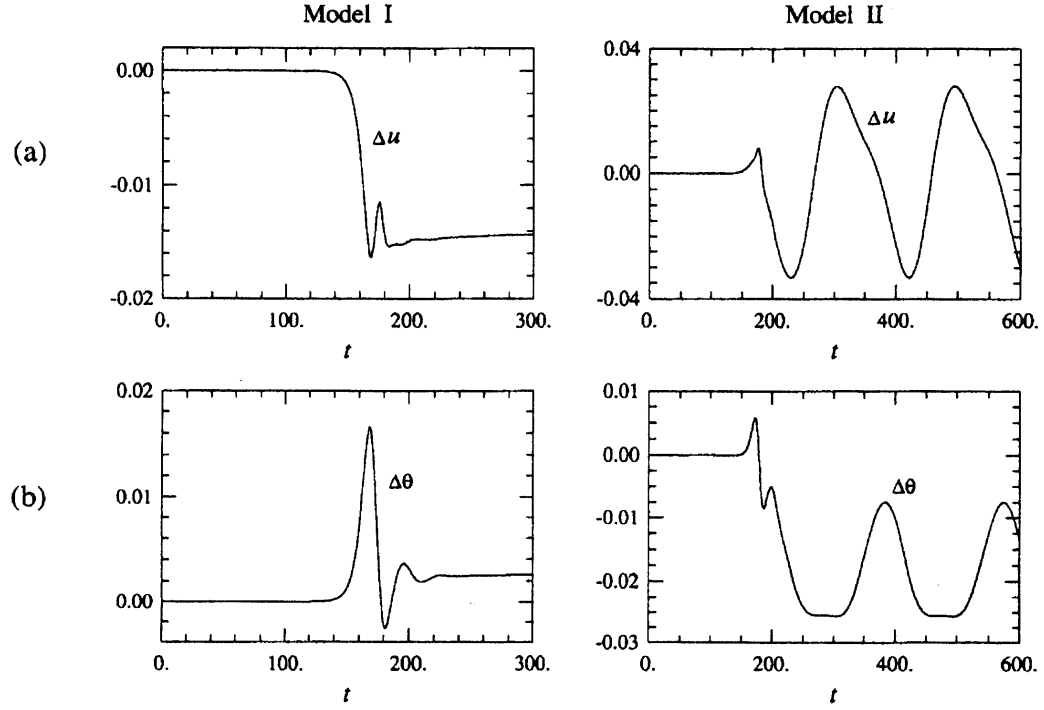

Fig. 5 Temporal behavior of local properties of the steady symmetric baroclinic waves (Ro =2.0, Pr =0.5): (a) zonal velocity, u; (b) temperature, θ, at a fixed location $y = L/2$ and z =-0.1964x10^{-1} for Model I (left column); $y = L/2$ and z =-0.51964 for Model II (right column).

Detailed structure of the steady symmetric baroclinic wave is now delineated. Fig. 6 illustrates the contour plots of zonal velocity, temperature and meridional streamfunction ψ for Model I under Ro=2.0, Pr=0.5. Here, ψ is defined as $v = \partial\psi/\partial z$, $w = -\partial\psi/\partial y$. Patterns of orderly development of symmetric baroclinic waves of finite wavelength are manifested. Since the upper and lower boundary conditions are identical, the temperature and zonal velocity of both the total and wave fields exhibit anti-symmetry about the mid-depth plane; positive deviations from the horizontally-averaged field in the upper zone correspond to negative deviations in the lower zone. The largest values of deviations are found near the edge of the Ekman boundary layers. The principal meridional motions consist of cells which are slightly tilted from the basic isotherms. As depicted in Fig. 6(f), both the counterclockwise (CCW) cells and the clockwise (CW) are visible. It is recalled that Pr<1 in this case. The implication is that the diffusive damping of the buoyancy effect is larger than the damping of the inertial effect. This results in the CW cells being of greater strength than the CCW cells.

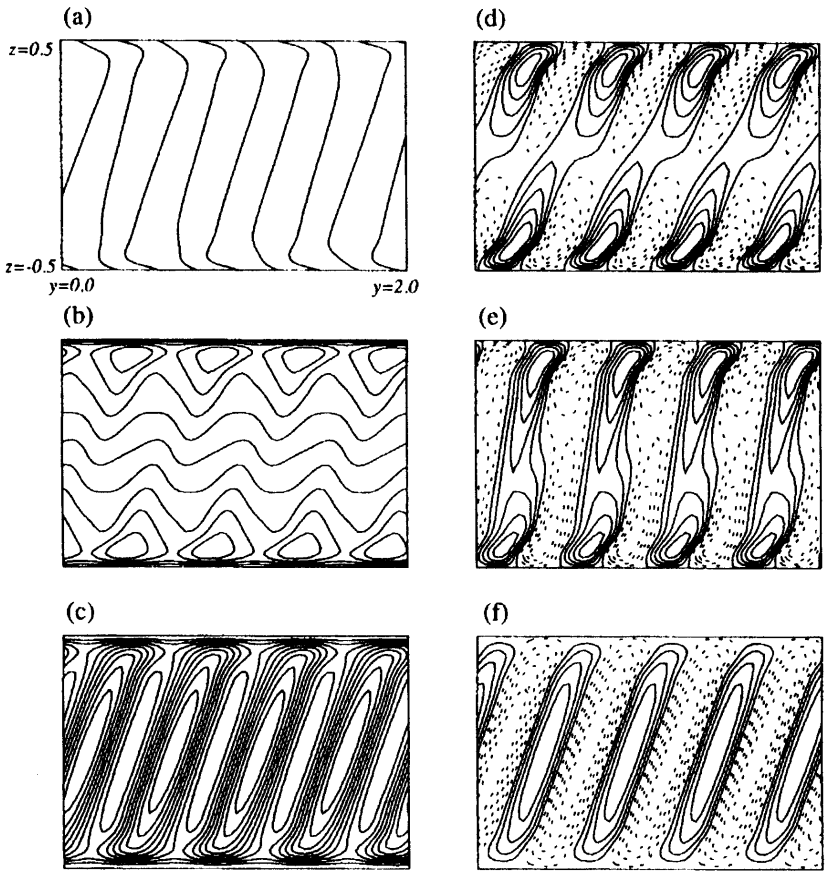

Fig. 6 Structures of the steady symmetric baroclinic waves of Model I (Ro =2.0, Pr =0.5): (a) temperature; (b) zonal velocity; (c) total streamfunction; (d) deviation temperature; (e) deviation zonal velocity; (f) deviation streamfunction. The maximum and minimum values are (a) $T_{max} = 0.1422$, $T_{min} = -2.192$; (b) $u_{max} = 0.2985$, $u_{min} = -0.2981$; (c) $\psi_{max} = 0.0$, $\psi_{min} = -8.544\times10^{-2}$; (d) $\theta'_{max} = 5.068\times10^{-2}$, $\theta'_{min} = -5.071\times10^{-2}$; (e) $u'_{max} = 6.559\times10^{-2}$, $u'_{min} = -6.547\times10^{-2}$; (f) $\psi'_{max} = 3.650\times10^{-3}$, $\psi_{min} = -3.927\times10^{-3}$. Contour increments are (Max.-Min.)/10 for all the figures. Dashed contours in frames (d), (e) and (f) indicate negative values.

Fig. 7 portrays the structures of steady symmetric baroclinic waves for Model II under Ro=2.0, Pr=0.5. Since the boundary conditions at the lower and upper walls are of different nature, anti-symmetry of the zonal velocity and of the temperature is not seen. However, the general features of the deviations of zonal velocity and of temperature are qualitatively similar to those of Model I.

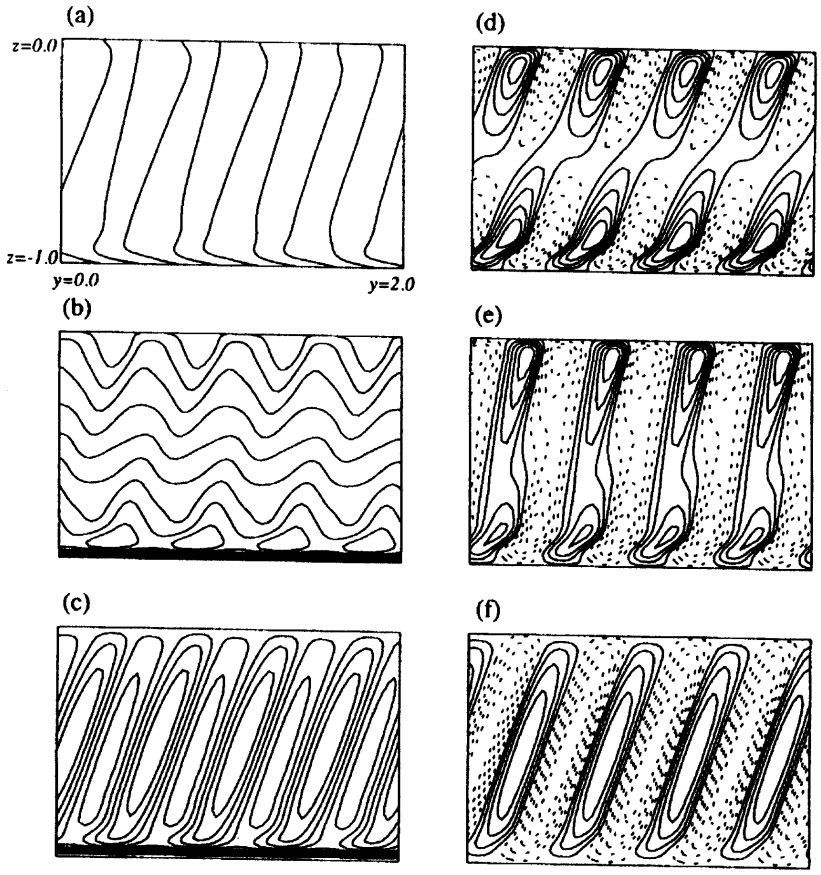

Fig. 7 Structures of the steady symmetric baroclinic waves of Model II (Ro=2.0, Pr=0.5). The maximum and minimum values are (a) $T_{max} = 0.0$, $T_{min} = -2.303$; (b) $u_{max} = 4.846\times10^{-2}$, $u_{min} = -0.5459$; (c) $\psi_{max} = 0.0$, $\psi_{min} = -1.201\times10^{-2}$; (d) $\theta'_{max} = 4811\times10^{-2}$, $\theta'_{min} = -4.3796\times10^{-2}$; (e) $u'_{max} = 7.624\times10^{-2}$, $u'_{min} = -6.593\times10^{-2}$; (f) $\psi'_{max} = 3.245\times10^{-3}$, $\psi_{min} = -3.497\times10^{-3}$. The legends are the same as in Figure 6.

In the next, the vacillating symmetric baroclinic wave regime is examined. As depicted in Fig. 3, this regime is tenable only in Model II under strongly-nonlinear situations, i.e., *Ro* is substantially large and *Ri* is appreciably smaller than Ri_C. Typical time-dependent characteristics of vacillating waves are illustrated in Fig. 8. It is apparent that time-varying fluctuations of the volume-averaged properties persist after the global equilibrium state is accomplished. The vacillations at large times are not interpreted to be residual oscillations of the first dominant mode of wave evolution in the afore-mentioned steady symmetric baroclinic wave regime. The vacillation pattern can be studied in further detail by analyzing the temporal variations of local properties at a fixed position, which are shown in Figs. 8(e) and 8(f). These pictures clearly point to the existence of several distinct oscillatory modes. As in steady symmetric baroclinic waves, the oscillation with the largest period is associated with the overall horizontal wave movement. The residual oscillation of wave evolution, which was seen for small *Ro*, is also discernible. On top of these, there exist different oscillatory modes of higher frequencies. Enlarged views of Figs. 8(e) and 8(f) are shown in Figs. 8(g) and 8(h); oscillations of shorter periods are visible in these pictures. It is obvious in Fig. 8 that the frequency of the most dominant oscillation is $O(2\Omega)$, which leads to the identification that this oscillation is at the inertial mode.

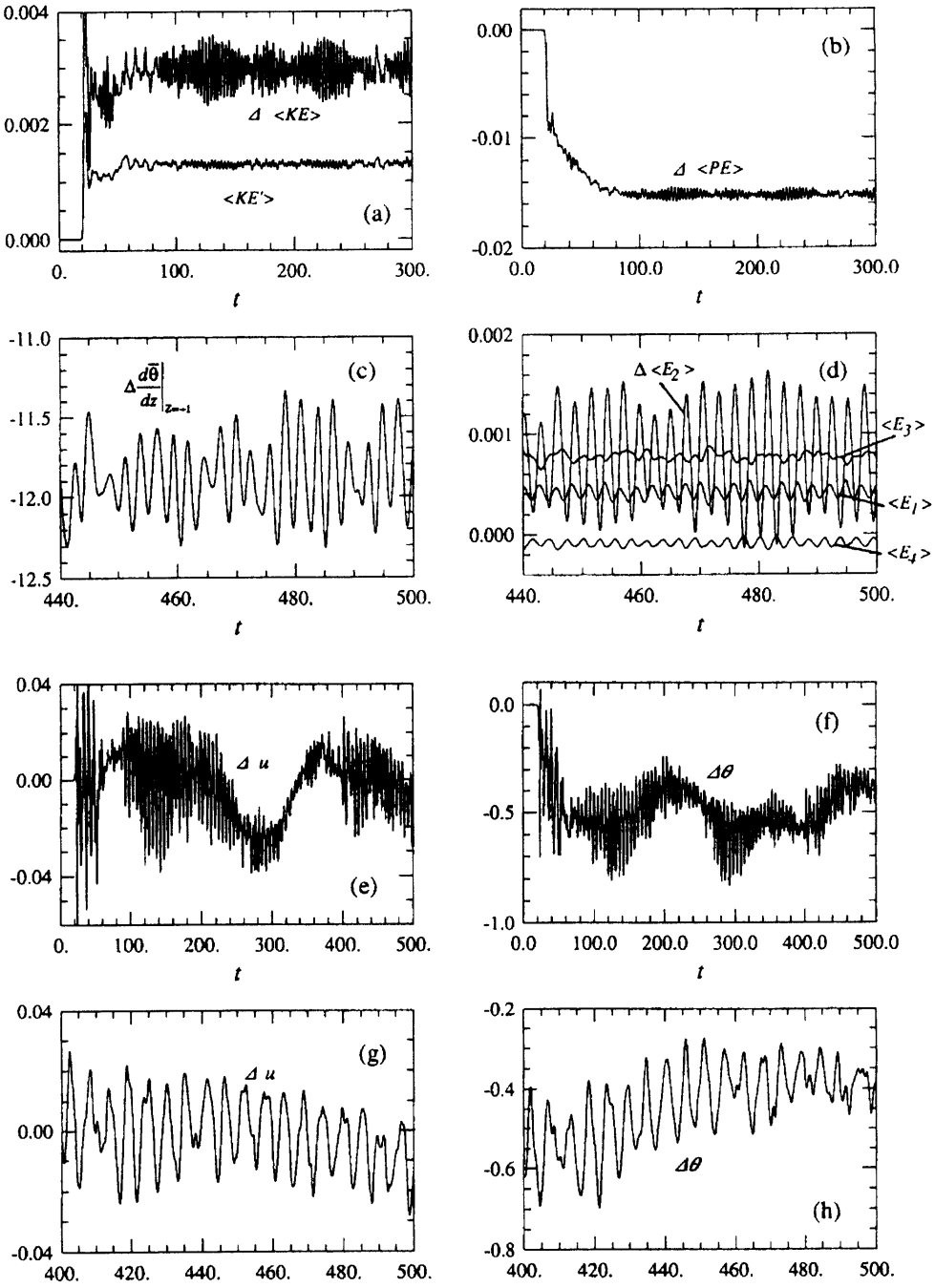

Fig. 8 Temporal behavior of the vacillating symmetric baroclinic waves of Model II (Ro=20.0, Pr=0.5). The legends for Figs. 8(a)-(d) and 8(e)-(f) correspond to those for Figs. 4 (a)-(d), and Figs. 5 (a)-(b), respectively. Figs. 8(g) and 8(h) are the enlarged views of Figs. 8(e) and 8(f).

Fig. 8(d) exhibits temporal vacillations of the equation terms in (19)-(22). The amplitude of fluctuation of $<E_2>$ is most vigorous in comparison to the other terms. This suggests that the flow vacillations are closely related to the fluctuation of heat transfer being advected into and out of the finite section of the channel via horizontal currents. It is important to recognize that the principal aspects of the energetics of the vacillating symmetric baroclinic wave regime remain qualitatively unchanged from those of the steady symmetric baroclinic waves. Despite the presence of

vacillations, $\langle E_2 \rangle$ and $\langle E_3 \rangle$ are dominant, and $\langle E_1 \rangle$ and $\langle E_4 \rangle$ are relatively small in magnitude (compare the mean values of these terms). This implies that the global energetics of the symmetric baroclinic waves are little affected by the time-dependent modes of waves and by the relative strength of the thermal forcing to the rotation effect, namely, the thermal Rossby number *Ro*. Rather, a major role to influence the energetics is played by the Prandtl number *Pr*, which measures the relative damping of the buoyancy effect to the inertial restoring effect. In the present problem setup, $Pr<1$ for all the cases which produce symmetric baroclinic waves. Consequently, the basic energetics exhibit qualitatively similar trends.

Fig. 9 demonstrates the structures of the vacillating waves. The formation of finite-amplitude symmetric waves is conspicuous, whether or not vacillations are present. At large *Ro*, the basic isotherms and the contours of zonal velocity tilt more to the horizontal than at small *Ro*. It is seen that maximum deviations of temperature and of zonal velocity are located near the upper boundary. This may be explained by noting that the free-slip and insulated upper boundary conditions provide insufficient viscous and thermal diffusion in this region, and this tends to be more pronounced for strongly nonlinear cases. As to the meridional flows, the interior is occupied by the CW and CCW cells of comparable magnitude. Each circulation cell is of different strength, which reflects the presence of flow vacillation, i.e., the strengths and shapes of CW and CCW cells vary with time.

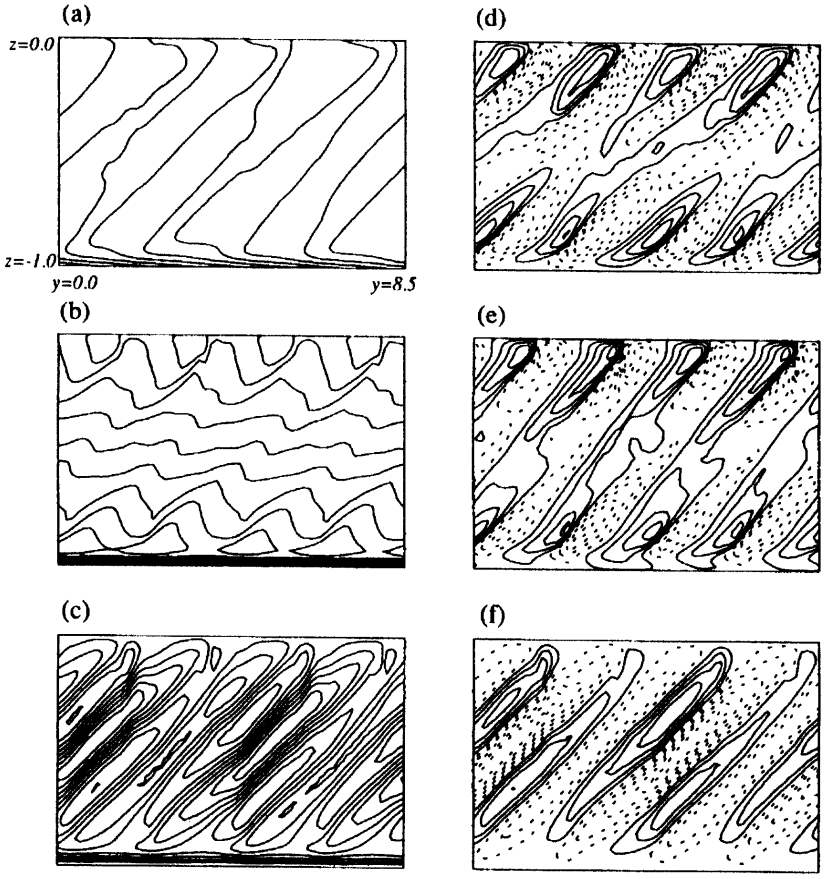

Fig. 9 Structures of the vacillating symmetric baroclinic waves of Model II (Ro=20.0 and Pr=0.5). The maximum and minimum values are (a) $T_{max} = 0.1970$, $T_{min} = -11.59$; (b) $u_{max} = 7.094\times10^{-2}$, $u_{min} = -0.5501$; (c) $\psi_{max} = 0.0$, $\psi_{min} = -1.639\times10^{-2}$; (d) $\theta'_{max} = 0.6848$, $\theta'_{min} = -0.7659$; (e) $u'_{max} = 8.081\times10^{-2}$, $u'_{min} = -0.1070$; (f) $\psi'_{max} = 6.472\times10^{-3}$, $\psi_{min} = -6.059\times10^{-3}$. The legends are the same as in Figure 6.

A perusal of Fig. 9 reinforces the earlier finding that the high-frequency vacillation in this flow

regime corresponds to the inertial mode. The classical treatise [1] states that the inertial instability arises when an unstable horizontal gradient of absolute angular momentum exists. In the present formulation based on an infinite channel model, angular momentum may not be defined in a strict sense, since the radial distance from the axis of rotation is not specifically defined. In order to examine inertial instability, an analogous angular momentum is introduceded, in nondimensional form, as

$$M = Ro \cdot u\text{-}2y \,. \tag{23}$$

Note that y increases toward the rotation axis and that a positive $\partial M / \partial y$ implies an inertially unstable situation. In Fig. 9(b), a large horizontal shear of zonal velocity is generated between the locations of maximum and of minimum deviations of zonal velocity near the upper boundary. The basic field is initially stable, i.e., $\partial M / \partial y = -2$, according to the definition of (23); however, a positive $\partial M / \partial y$ can be produced in the wave field due to the presence of a positive horizontal shear of zonal velocity. This assertion has added significance for the cases of large Ro. It is clearly shown that an inertially unstable zone exists near the upper boundary. In Figs. 9(g) and 9(h), the amplitude of inertial oscillations changes with a characteristic time scale of $O(E^{-1/2})$. These changes are based on the propagation of inertial instability, initiated in the upper boundary zone, into the interior by the actions of meridional circulations.

Summarizing the above computed features, a physical explanation emerges to the question of why vacillating waves are discernible for Model II, but not for Model I. For Model II, the areas in which the deviations of zonal velocity are most vigorous, are located near the free-slip upper boundary, not in the interior. On the other hand, for Model I, the viscous damping in the Ekman layers suppresses the inertial instability near the no-slip horizontal boundary walls. Miller [*4*] stated that chaotic flows were seen in strongly nonlinear situations, and he conjectured that this may be due to the sharp front of shear (i.e., the inertial instability) or the thermal convective instability. The above-illustrated numerical data of the present simulations point to the latter mechanism as the cause of the non-diminishing unsteadiness.

It is of interest to note that, in the present simulations, no evidence was found for the occurrences of the standard Benard-type instability associated with a negative vertical temperature contrast in the Ekman layer [*19,20*]. For the original Hadley cell model [*4*], this kind of instability was reported to take place for certain parameter ranges, especially for large Ro and Pr. In the present work, for all the runs which produced symmetric baroclinic waves, $Pr<1$. Based on the present results, it is asserted that the appreciable thermal diffusive damping overturns the Benard-type instability in the thermal boundary layer.

Finally, discussions will be focused on the impact of the nonlinear (and/or finite-amplitude) effects of symmetric baroclinic wave formation on the basic-state flow field. For this purpose, vertical profiles of the horizontally-averaged zonal and meridional velocity components are useful. Fig. 10 demonstrates such plots for Model II, together with the basic-state profiles. It is readily recognized that the horizontally-averaged velocity field is not significantly affected by the presence of waves. A slight invigoration of the horizontally-averaged zonal velocity is seen near the boundary layers, which serves to intensify the meridional flow in these regions. When Ri is far below Ri_C, the horizontally-averaged meridional velocity field in the interior is distorted to some extent. This can be attributable to vigorous nonlinear advections of the wave momentum. Also, the main part of the $<E_2>$ term, which represents conversion from the potential energy to the horizontally-averaged kinetic energy, is accomplished in these regions. However, inspection of the horizontally-averaged velocities indicates that the overall impact of the presence of the wave is minor throughout the fluid layer. Alternatively speaking, the finite-amplitude effects, which are appreciable when Ri is much lower than Ri_C, are not conspicuous in the horizontally-averaged

velocity fields. These observations are common to both Models I and II for small and large *Ro*.

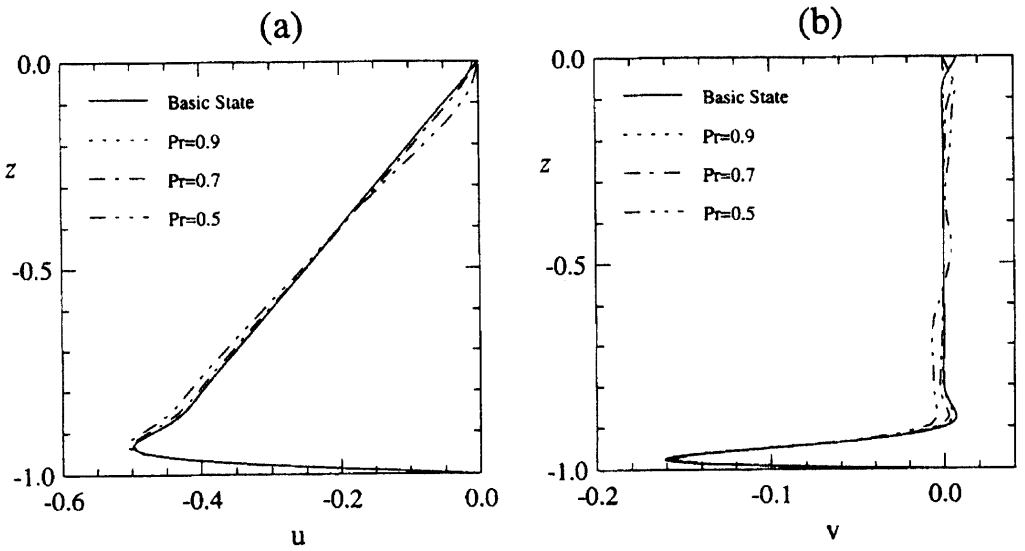

Fig. 10 The horizontally-averaged velocities of Model II with Ro =20.0 : (a) zonal velocity, (b) meridional velocity.

The influence of the presence of the wave is not insignificant for the horizontally-averaged temperature field. Fig. 11 illustrates that, for varying Pr and fixed Ro, the difference between temperatures of the horizontally-averaged field and of the basic state is considerable, as the finite-amplitude symmetric baroclinic waves are generated (recall that the basic-state temperature scaled by $RoPr/2$ is a function of E only). When Ri is slightly less than Ri_C, this difference is small. However, this difference increases as Ri/Ri_C decreases, which results in an increase of the static stability (positive vertical temperature gradient) of the interior fluid. This qualitative feature is visible for both models and for all values of Ro.

Another interesting aspect of the present findings is that the vertical temperature gradient increases roughly in proportion to $(Ri_C - Ri)$. To exemplify this assertion, Fig. 12 displays the vertical profiles of the horizontally-averaged temperature, scaled by $Ro/4$. It is clear that the vertical gradients of the horizontally-averaged temperatures in the interior remain virtually unchanged for the case of Ri_C, as Pr takes different values. It is recalled that, in the present Models I and II, the basic-state temperature is a linear function of Pr. The numerical results suggest that, when symmetric baroclinic waves are present, the gradient of the horizontally-averaged temperature profile is quite insensitive to the variation in Pr.

As remarked earlier, the vertical shear of the horizontally-averaged zonal velocity in the interior remains unchanged from the value 1/2. Consequently, the resultant Richardson number may be written as $Ri = 4\,/Ro/(\partial\bar{\theta}/\partial z)$. The slopes of the curves in the interior, as shown in Fig. 12, are nearly identical to the resultant Richardson number Ri after the waves are formed, in accordance with the above expression. It can be seen that, in view of the above development, the numerical value of the resultant Ri is nearly the same as Ri_C for a fixed Ro. Physical descriptions of this aspect are revealing : as SBI is triggered, it works to narrow the difference between Ri_C and the resultant Richardson number of the flow. Based on this physical argument, it can be ascertained that, after symmetric baroclinic waves are generated, the value of Ri_C for a particular value of Ro may be estimated from the value of the resultant Ri of the horizontally-averaged flow field. These physical pictures are equally applicable to both Models I and II. The difference is that, for Model II, due to the free-slip and insulated upper boundary conditions, the overall profiles of the horizontally-averaged temperatures are shifted further to the right (the fluid temperature in the interior

increases), as Ri/Ri_C decreases. This reduces negative vertical temperature gradients in the lower boundary layer. This also is supportive of the contention that, in Model II, the conventional Benard-type convective instability, which is associated with a negative vertical temperature difference in the thermal boundary layer, is less likely to occur than in Model I.

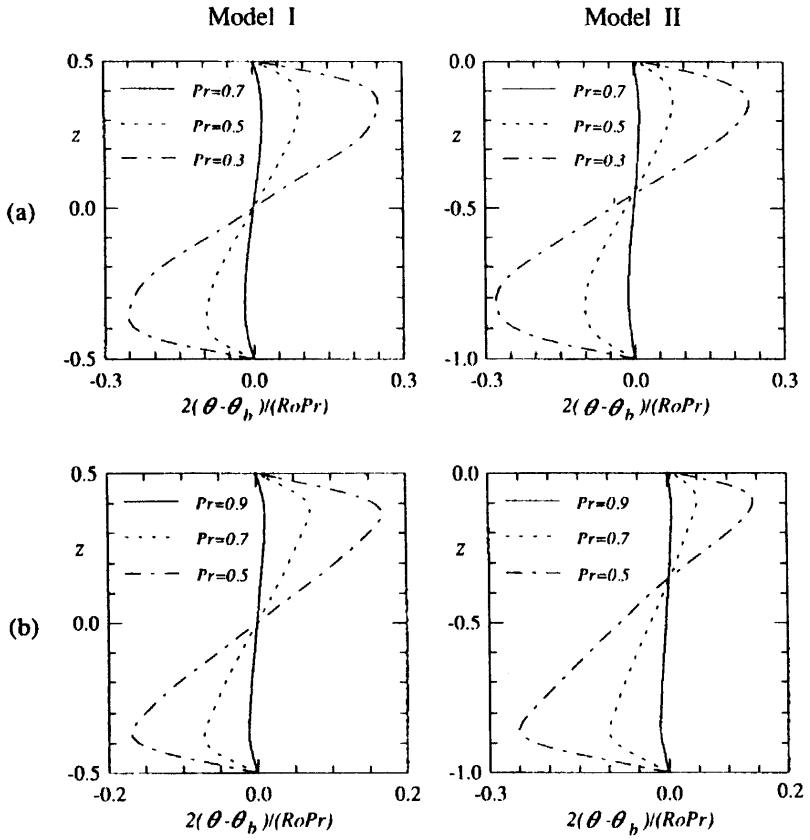

Fig. 11 Deviations of the horizontally-averaged temperature from the basic state: (a) for Ro =2.0; (b) for Ro =20.0. The left and right columns are for Models I and II, respectively. Note that subscript b denotes the basic-state temperature.

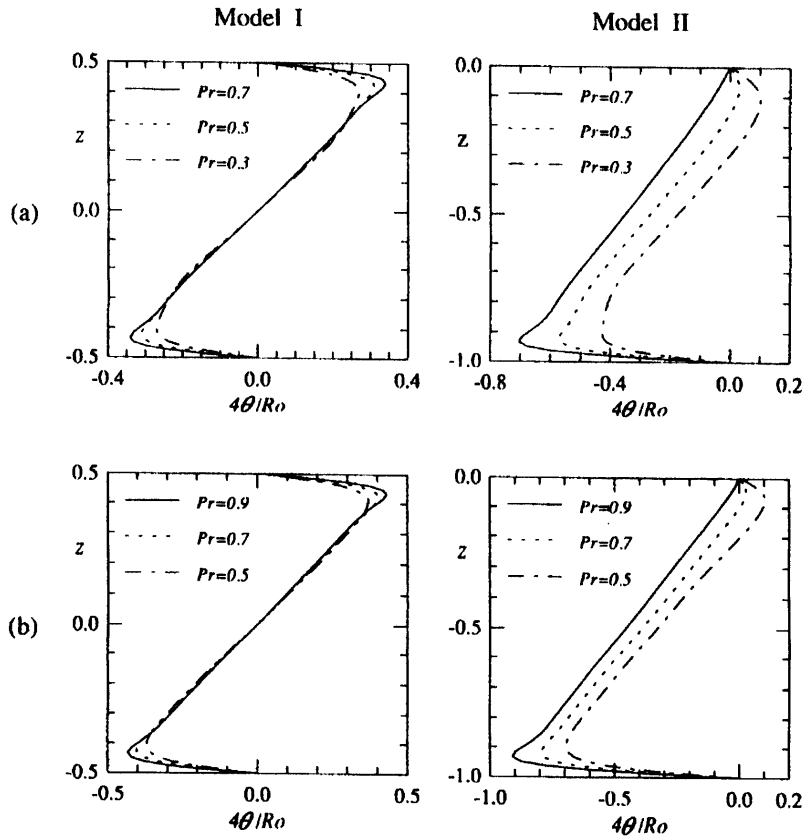

Fig. 12 Vertical profiles of the horizontally-averaged temperature, scaled by $Ro/4$: (a) for Ro =2.0; (b) Ro =20.0. The left and right columns are for Models I and II, respectively.

4. CONCLUSION

The regime diagram in the *Ri-Ro* plane discloses three major categories, i.e., (1) the regime of stable flow to SBI, (2) the steady finite-amplitude symmetric baroclinic wave regime, and (3) the vacillating symmetric baroclinic wave regime. The overall shapes of the stability curves for Models I and II are consistent with the results of the Eady model. Since the upper boundary wall of Model II is insulating, Model II appears to be more stable to SBI than Model I for small *Ro*.

The large-time behavior shows that the wave generation is closely associated with the enhanced heat transfer to the fluid. Both the horizontally-averaged and wave kinetic energies grow at the expense of potential energy.

The local properties for Model II displays oscillatory patterns, however, the oscillatory tendency for Model I at large times is less conspicuous. Detailed structures of the steady symmetric baroclinic wave for Model I exhibit anti-symmetry about the mid-depth plane. Due to the free-slip upper boundary wall, wave structures for Model II do not display anti-symmetry.

The vacillating symmetric baroclinic wave regime is shown to be tenable for Model II in a strongly-nonlinear situation. The dominant oscillation is identified to be at the inertial mode. The principal features of the energetics of the vacillating symmetric baroclinic wave regime remain unchanged from those of the steady symmetric baroclinic waves. For Model I, viscous damping in the Ekman layers suppresses the inertial instability near the no-slip horizontal boundary walls. In the case of Model II, deviations of the zonal velocity are most vigorous near the free-slip upper boundary.

The finite-amplitude effects are not conspicuous in the horizontally-averaged velocity fields, for both Models I and II. However, the presence of the wave affects significantly the horizontally-averaged temperature field. When symmetric baroclinic waves are present, the gradient of the horizontally-averaged temperature profile is insensitive to the variations in Pr. The numerical results indicate that the conventional Benard-type convective instability is less likely to occur in Model II than in Model I.

REFERENCES

[1] ROBERTS, P. H. and SOWARD, A. M., *Rotating Fluids in Geophysics*, Academic Press, London, (1978).

[2] ANTAR, B. N. and FOWLIS, W. W.: Symmetric Baroclinic Instability of a Hadley Cell, *J. Atmos. Sci.* vol. **39**, pp. 1280-1289 (1982).

[3] ANTAR, B. N. and FOWLIS, W. W.: Three-Dimensional Baroclinic Instability of a Hadley Cell for Small Richardson Number, *J. Fluid Mech.* vol. **137**, pp. 423-445 (1983).

[4] MILLER, T. L.: The Structures and Energetics of the Fully Nonlinear Symmetric Baroclinic Waves, *J. Fluid Mech.* vol. **142**, pp. 343-362 (1984).

[5] MILLER, T. L.: On the Energetics and Nonhydrostatic Aspects of Symmetric Baroclinic Instability, *J. Atmos. Sci.* vol. **42**, pp. 203-211 (1985).

[6] STONE, P. H.: An Application of Baroclinic Stability Theory to the Dynamics of the Jovian Atmosphere, *J. Atmos. Sci.* vol. 24, pp. 642-652 (1967).

[7] BENNETS, D. A. and HOSKINS, B. J.: Conditional Symmetric Baroclinic Instability a Possible Explanation for Frontal Rainbands: *Quart. J. Roy. Meteor. Soc.* vol. **105**, pp. 945-962 (1979).

[8] EMANUEL, K. A.: Inertial Instability and Mesoscale Convective Systems. Part I: Linear Theory of Inertial Instability in Rotating Viscous Fluids, *J. Atmos. Sci.* vol. **36**, pp. 2425-2449 (1979).

[9] MILLER, T. L. and ANTAR, B. N.: Viscous Nongeostrophic Baroclinic Instability, *J. Atmos. Sci.* vol. **43**, pp. 329-338 (1986).

[10] THORPE, A. J. and ROTUNNO, R.: Nonlinear Aspects of Symmetric Instability, *J. Atmos. Sci.* vol. **46**, pp. 1285-1299 (1989).

[11] STONE, P. H.: On Nongeostrophic Baroclinic Stability, *J. Atmos. Sci.* vol. **23**, pp. 390-400 (1966).

[12] STONE, P. H.: Baroclinic Stability under Non-Hydrostatic Conditions, *J. Fluid Mech.* vol. **45**, pp. 659-671 (1971).

[13] MCINTYRE, M. E.: Diffusive Destabilization of the Baroclinic Circular Vortex, *Geophys. Fluid Dynam.* vol. **1**, pp. 19-57 (1970).

[14] ANTAR, B. N. and FOWLIS, W. W.: Baroclinic Instability of a Rotating Hadley Cell, *J. Atmos. Sci.* vol. **38**, pp. 2130-2141 (1981).

[15] HIDE, R. and MASON, P. J.: Sloping Convection in a Rotating Fluid, *Adv. Phys.* vol. **24**, pp. 47-100 (1975).

[16] STONE, P. H., HESS, S., HADLOCK, R., and RAY, P.: Preliminary Results of Experiments with Symmetric Baroclinic Instabilities, *J. Atmos. Sci.* vol. **26**, pp. 991-996 (1969).

[17] HADLOCK, R. K., NA, J. Y. and STONE, P. H.: Direct Thermal Verification of Symmetric Baroclinic Instability, *J. Atmos. Sci.* vol. **29**, pp. 1391-1393 (1972).

[18] MILLER, T. L. and FOWLIS, W. W.: Laboratory Experiments in a Baroclinic Annulus with Heating and Cooling on the Horizontal Boundaries, *Geophys. Astrophys. Fluid Dynam.* vol. **34**, pp. 283-300 (1986).

[19] HATHAWAY, D. H. and FOWLIS, W. W.: Flow Regimes in a Shallow Rotating Cylindrical Annulus with Temperature Gradients Imposed on the Horizontal Boundaries, *J. Fluid Mech.* vol. **172**, pp. 401-418 (1986).

[20] QUON, C.: Quasi-Steady Symmetric Regimes of a Rotating Annulus Differentially Heated on the Horizontal Boundaries, *J. Atmos. Sci.* vol. **37**, pp. 2407-2423 (1980).

[21] PATANKAR, S. V.: *Numerical Heat Transfer and Fluid Flow*, McGraw-Hill, New York, (1980).

[22] HAYASE, T., HUMPHREY, J. A. C. and GRIEF, R.: A Consistently Formulated QUICK Scheme for Fast and Stable Convergency Using Finite-Volume Iterative Calculation Procedures, *J. Comp. Phys.* vol. **98**, pp. 108-118 (1992).

[23] KWAK, H. S. and HYUN, J. M.: Baroclinic Waves in a Shallow Rotating Annulus with Temperature Gradients Imposed on the Horizontal Boundaries, *Geophys. Astrophys. Fluid Dynam.* vol. **66**, pp. 1-23 (1992).